Al–Ge–Al nanowire heterostructure: from single-hole quantum dot to Josephson effect

Jovian Delaforce, Masiar Sistani, R. B. G. Kramer, Minh Luong, Nicolas Roch, Walter Weber, Martien den Hertog, Eric Robin, Cecile Naud, Alois Lugstein, et al.

To cite this version:

Jovian Delaforce, Masiar Sistani, R. B. G. Kramer, Minh Luong, Nicolas Roch, et al.. Al–Ge–Al nanowire heterostructure: from single-hole quantum dot to Josephson effect. Advanced Materials, 2021, 33 (39), pp.2101989. ⟨10.1002/adma.202101989⟩. ⟨hal-03348045⟩

HAL Id: hal-03348045
https://hal.science/hal-03348045v1

Submitted on 5 Oct 2021

Al-Ge-Al nanowire heterostructure: from single hole quantum dot to Josephson effect

Jovian Delaforce[1#], *Masiar Sistani*[2#], *Roman B. G. Kramer*[1], *Minh A. Luong*[3], *Nicolas Roch*[1]

Walter M. Weber[2], *Martien I. den Hertog*[1], *Eric Robin*[3], *Cecile Naud*[1], *Alois Lugstein*[2],

Olivier Buisson[1*]

#These authors contributed equally.

Mr. J. Delaforce, Dr. R. B. G. Kramer, Dr. N. Roch, Dr. M. I. den Hertog, Dr. C. Naud, Dr. O. Buisson
Université Grenoble Alpes, CNRS, Institut NEEL UPR2940, Grenoble, 38042, France
Email: olivier.buisson@neel.cnrs.fr

Dr. M. Sistani, Prof. W. M. Weber, Aso. Prof. A. Lugstein
Institute of Solid State Electronics, TU Wien, Gußhausstraße 25-25a, Vienna, 1040, Austria

Dr. M. A. Luong, Dr. E. Robin
Université Grenoble Alpes, CEA, IRIG-DEPHY, F-38054 Grenoble, 38054, France

Keywords: nanowire heterostructure, quantum dot, germanium, superconductor-semiconductor hybrids, Josephson field-effect transistor

Abstract

Superconductor-semiconductor-superconductor heterostructures are attractive for both fundamental studies of quantum phenomena in low dimensional hybrid systems as well as for future high-performance low power dissipating nanoelectronic and quantum devices. Within this paper, ultra-scaled monolithic Al-Ge-Al nanowire heterostructures featuring monocrystalline Al leads and abrupt metal-semiconductor interfaces are used to probe the low-temperature transport in intrinsic Ge (i-Ge) quantum dots. In particular, demonstrating the ability to tune the Ge quantum dot device from completely insulating, through a single hole filling quantum dot regime, to a supercurrent regime, resembling a Josephson field effect transistor with a maximum critical current of 10 nA at a temperature of 390 mK. The realization of a Josephson field-effect transistor with high junction transparency provides a mechanism to study sub-gap transport mediated by Andreev states. The presented results reveals a promising intrinsic Ge based architecture for hybrid superconductor-semiconductor devices for the study of Majorana zero modes and key components of quantum computing such as gatemons or gate tuneable SQUIDS.

1. Introduction

The coupling of two well-established systems, superconducting circuits and quantum dots (QDs), to create hybrid devices has conceived a new and promising domain. The amalgamation of the superconducting proximity effect of the superconducting leads and the well-defined electronic states of the QD results in mesoscopic quantum devices with broad applications and rich physics.[1] Hybrid junctions have been realised with various architectures using a wide range of materials, with significant focus on carbon nanotubes[2,3] graphene[4,5] or high mobility compound semiconductors such as InSb[6,7] or InAs/InP[8–11] nanowires (NWs). These research efforts continue to highlight the richness and applicability of hybrid junctions with experiments showing interesting results, beyond Coulomb blockade (CB) and tunable supercurrent, including Kondo physics, Andreev Bound States (ABS), and possible signatures of Majorana fermions.[6] Extending the architecture by the possibility to modulate the QD electrostatically, hybrid systems also resemble Josephson field-effect transistors which can be integrated into quantum devices including tunable superconducting quantum interference devices (SQUIDs)[1,12] and gated superconducting qubits (gatemons) for sensing and quantum computing applications respectively.[13]

Recently quantum devices based on confined Ge nanostructures have seen a growth in interest due to exceptional material properties and compatibility with mature CMOS processes. In particular, due to its large hole mobility, strong spin orbit coupling and tunable g-factors, Ge is promising for both spin qubit control and, specific to hybrid junctions, for the observation of Majorana zero modes required for topological quantum computing. Ge is predominantly integrated with Si in the form of Ge/Si core/shell NW junctions[14–17] Ge/Si planar junctions[18,19] or Ge hut wires[20] with Si caps. However, proximity induced superconductivity in intrinsic Ge (i-Ge) channels remains elusive. This is mainly associated with the difficulty in overcoming the metal-Ge Schottky barrier which, despite forming close to the valence band due to Fermi level pinning,[21] can prevent proximity induced supercurrent. Overcoming the Schottky barrier requires the fabrication of high quality electrical contacts to Ge nanostructures while simultaneously reducing the gate screening effect of the leads.[22,23] This tremendous challenge has been recently achieved through intense research on the thermal diffusion of metals into semiconducting NWs.[24–26] The absence of an intermetallic phase formation and compatible diffusion rates between Al-Ge have been exploited extensively to form true metal-Ge heterostructures with abrupt interfaces[27–30] leading to the formation–of self-aligned Al NWs contacting the monolithically integrated Ge QD.

In this article, we use such monolithic and single-crystalline Al-Ge-Al NW heterostructures integrated into a back gated field-effect device to investigate low-temperature transport of an ultra-scaled i-Ge QD embedded between two superconducting Al leads. By controlling a single gate voltage, we can adjust the system to a variety of quantum transport regimes. The transport regimes of a hybrid device are defined by its dominant energy scales: the superconducting gap (Δ), the tunnel coupling (Γ) and the charging energy (E_C).[1] Most devices are limited to a single transport regime of interest depending on its characteristic energies and gate tunability, which are determined during fabrication with or without intention.[10,18] In the actual Al-Ge-Al device, Γ and E_C can be tuned via the single back gate providing access to different transport regimes in a single device. Here we will detail the properties of the three major regimes: first, the *weak coupling regime* ($\Gamma << \Delta << E_C$) where we observe CB with large E_C, strong confinement effects and single hole filling. Second, the *intermediate coupling regime* ($\Gamma \sim \Delta \sim E_C$) where superconducting sub-gap resonances appear related to resonant effects between Andreev and QD states. Finally, the *strong coupling regime* where the pure Ge segment exhibits proximitized superconductivity with a tunable supercurrent extending to 10 nA and remarkable channel transparencies up to 95%. The observation of supercurrent through the i-Ge segment adds monolithic Al-Ge-Al nanowire heterostructures to the field of Ge based superconducting hybrid junctions.

2. Results and Discussion

2.1 Fabrication of ultra-scaled Al-Ge-Al NW devices

The Al-Ge-Al NW heterostructures have been fabricated by a thermally induced exchange reaction between vapor-liquid-solid grown single-crystalline undoped i-Ge NWs enwrapped in a 20 nm Al_2O_3-shell and lithographically defined Al contact pads (see **Figure 1.**a).[27,31] This technique enables the fabrication of ultra-short Ge segments contacted by self-aligned, quasi-1D, crystalline Al leads.[25,32] By this method Ge lengths as short as 10 nm are realized,[26] well beyond lithographic limitations (see Supplementary Information (SI) for details). The rodlike structure prevents the usual screening of the gate electric field due to large lithographically defined contacts and enables excellent electrostatic control of field effect devices.

The Al-Ge-Al NW heterostructures are integrated in a back-gated field-effect transistor architecture using a heavily p-doped Si substrate with a 100 nm thick SiO_2 dielectric layer. To investigate the structural properties as well as the Al-Ge interface quality, devices identical in construction have been fabricated on 40 nm thick Si_3N_4-TEM-membranes.[33] Figure 1.b shows that the exchange reaction forms an Al-Ge-Al NW heterostructure while maintaining a uniform diameter and abrupt interface. A zoom on the Al-Ge interface (Figure 1.c) reveals that the interface is nearly atomically sharp with the Ge lattice oriented along the [110] direction, transitioning to crystalline Al (c-Al) in a single atomic layer. More details regarding the principal heterostructure formation mechanism including STEM/EDX investigations are discussed in the SI and supplied in the papers of Kral et al.[27] and El Hajraoui et al..[31]

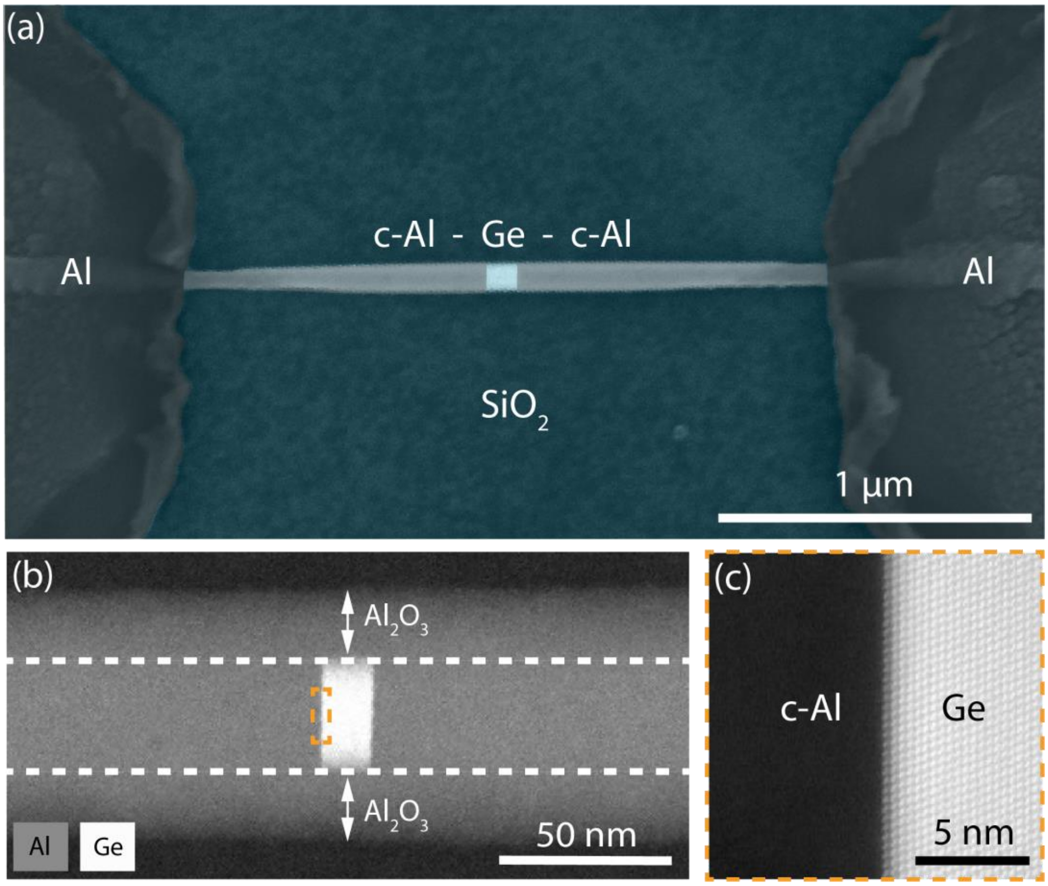

Figure 1. (a) False color SEM image of an Al-Ge-Al NW heterostructure integrated in a back-gated field-effect transistor architecture. (b-c) High-resolution high angle annular dark field (HAADF) scanning transmission electron microscopy (STEM) image using a probe corrected FEI Titan Themis working at 200 kV of (b) a 15 nm long Ge segment embedded in an Al-Ge-Al NW heterostructure. (c) of the abrupt Al-Ge interface of the Al-Ge-Al NW heterostructure orientated along the [110] direction.

2.2 Overview of Transport Properties

Two devices (samples 1 and 2) have been measured with a core NW diameter of 25 nm and a Ge segment length of 42 nm and 37 nm, respectively. In previous work on similar devices with longer Ge segments the room temperature mobility was estimated to be 370 $cm^2V^{-1}s^{-1}$.[34] The lower mobility of Ge NWs compared to bulk Ge is associated with their significant surface scattering.[35–37] This mobility is half of the reported mobility of 730 $cm^2V^{-1}s^{-1}$ in

Ge/Si core/shell NWs with comparable diameters.[38] This higher mobility is explained by the hole gas which forms in the Ge core due to the band discontinuity between Ge and the Si shell.

Figure 2.a-b show the differential conductance, in units of quantum conductance, versus bias voltage (V_D) of sample 1 and 2 recorded at T = 390 mK and 410 mK respectively over an extended gate voltage (V_G) region. The two measured devices display similar highly tuneable transport properties with four distinguishable regimes: 1) a full blockade regime for $V_G > 0.5$ V, 2) a CB regime from the first hole to a few tens of holes in the QD (-4.5 V $< V_G < 0.5$ V), 3) an intermediate regime with various sub-gap features (-15 V $< V_G < -4.5$ V) and 4) a supercurrent regime at very negative gate voltages. We also observe peaks in conductance due to Andreev reflections at $eV = 2\Delta/n$, where n is the order of reflection. As discussed in by Sistani et al.[28] the tunnel barriers for the actual device are defined by weak Schottky barriers for holes resulting from the combination of Fermi level pinning due to Ge surface states and band correction due to the metal/semiconductor contact. Former investigations on Al-Ge-Al heterostructures with long Ge segments,[29] have shown that the gate voltage strongly modifies the valence band and Schottky barrier profile. The intrinsic coupling of the charge density and Schottky barrier, enables one to simultaneously tune E_C and Γ by modulating the back gate voltage.

Comparing to estimates of the room temperature mean-free path of $\ell_{Ge} = 45$ nm[25] these devices are on the margin between the ballistic and diffusive regimes. This explains why clear quantized conductance, expected for few channel ballistic semiconductors, was not observed in the normal regime (see supporting Figure S4). Given the strong similarity between the samples we will discuss these regimes hereafter using the electrical transport measurements of mainly sample 1.

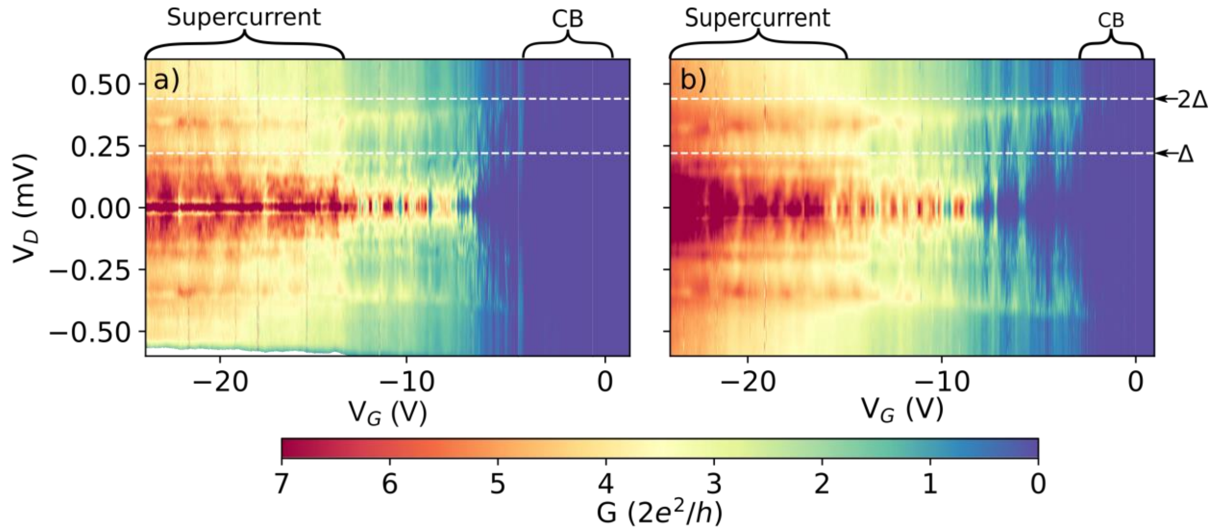

Figure 2. Density plot of differential conductance versus bias voltage (V_D) and gate voltage (V_G) of (a) sample 1 measured at 390mk and (b) sample 2 measured at 410mK. We observe four distinct regimes: A full blockade regime for $V_G > 0.5$ V. A Coulomb blockade (CB) regime (-4.5 V < V_G < 0.5 V), labelled, an intermediate regime (-15 V < V_G < -4.5 V) and a supercurrent regime (V_G < -15 V), labelled. Horizontal dashed lines show the expected position ($eV_D = 2\Delta/n$) of the first two conductance peaks due to Andreev reflection for $\Delta = 220$ µeV.

2.3 Weak coupling regime

Figure 3.a-b-c show stability diagrams of the conductance versus V_D over V_G range of -3.75 V < V_G < 0.4 V at 390 mK. We observe clear diamond shaped structures which points to CB suggesting that the device acts as a QD with single hole filling. Charge degeneracy points[39] occur when a charge state of the QD is in resonance with both chemical potentials of the leads allowing charge tunneling into and out of the QD. In the stability diagrams, these points manifest themselves as the juncture of the diamond edges of the N and N-1 charge states, where N is the number of holes on the QD. In Figure 3.a, we observe the first charge degeneracy point at $V_G = 0.224$ V. The current pinch-off observed for $V_G > 0.274$ V and

measurements up to V_G = + 5 V revealing for both samples that current is completely blocked suggests that we are observing the introduction of the first hole in the QD at V_G = 0.224 V. We estimate the number of holes inside the QD by counting the number of charge degeneracy points (see Figure 3). Although the occurrence of charge jumps during the measurement causes uncertainty, we estimate that this number is accurate to +/- 2. The presence of a superconducting gap in the density of states of the leads results in the charge degeneracy resonances occurring at a non-zero bias voltage of eV_D = +/- 2Δ as clearly visible on Figure 3.c. The voltage gap between the diamond peaks is approximately 0.88 mV +/-0.02 mV, which corresponds to Δ = 220 +/- 10 μeV which is consistent with the observed gap in QD devices with Al contacts.[29,40] Further, the measured Δ agrees with the BCS gap of 222 μeV measured from a critical temperature of T_C = 1.46 K. This T_C was determined for a pure c-Al nanowire where all the Ge had diffused out of the nanowire and into the bulk Al pads.[41] Hereafter, references to the gap are associated with the superconducting gap and not the semiconducting band gap of Ge.

We show in Figure 3.d a plot of the current I_D versus V_G, by taking voltage bias slices at V_D = 0.48 mV (see SI for details). The plot reveals periodic current peaks separated by near-zero current regions typical of CB. Figure 3.d also highlights the significant tunability of the QD's conductance: the first current peak, at V_G = 0.224 V, has a magnitude of approximately 5 pA whereas the final current peak at V_G = -3.645 V has a magnitude of approximately 1 nA. In the blockade regions, the current increases from zero to 0.4 nA around V_G = -3.6 V. The evolution of the current can be associated with the decreasing strength of the Schottky barrier as V_G decreases. To quantify this evolution we estimate Γ (see SI for details) for charge states N = 2, 17, 24 and 31 obtaining Γ = 6.2, 82, 102 and 250 μeV, respectively. Comparing to 3 meV < E_C < 32 meV and Δ = 220 μeV we conclude that the QD is in the weak coupling regime until $V_G \approx$ - 3.7 V.

Interestingly, as Γ becomes comparable to the superconducting gap ($\Gamma \sim \Delta < E_C$), a zoom on the superconducting gap reveals sub-gap conductance resonances which meet at $eV_D \approx +/-\Delta$ occur at the charge degeneracy points (see SI). These sub-gap features are mediated by Andreev reflections and will be discussed in more detail in the next section.

Figure 3e shows the addition energy, $E_{add}(N)$, the energy required to introduce the N^{th} hole to the QD containing N-1 holes versus V_G. E_{add} is defined as the sum of $E_C = e^2/(C_S + C_D + C_G)$ where C_S, C_D, and C_G are the source, drain and gate capacitances and the single particle level spacing (δ_1) which is dependent on the valence band states of the QD. The SI provides a detailed discussion of the calculation of $E_{add}(N)$. As shown on Figure 3.d, in the few hole regime (N<10) E_{add} is sporadic moving between 3 and 17 meV. With approximately 10 holes in the QD, E_{Add} begins to decay steadily until N ≈ 20 where it converges into an odd-even hole filling effect. From the odd-even filling effect, affirmed in the SI, the δ_1 in the many hole regime is estimated to be 1.0 +/- 0.3 meV. We associate the evolution of E_{add} to the evolution of E_C already observed in long Ge segment heterostructures:[29] as V_G decreases the valence band shifts further above the Fermi energy, increasing the size of the QD, thus increasing the magnitude of C_S and C_D.

A demonstration of strong confinement in the QD is the observation of resonant tunneling through excited charge states, which manifest as conductance lines that run parallel to diamond edges. We observe such features throughout the stability diagram. From the conductance features at V_G = -1.53 V with N ≈ 12, we calculate the energy of the first excited hole state to be ΔE = 2.0 meV (see SI for details). Whereas, in the many hole regime (N > 20) the average energy of the observed first excited states is 1.2 +/- 0.6 meV, which agrees with δ_1 estimated from the odd-even effect. Using a general expression for the energy spacing due to quantum confinement $\Delta E \sim h^2/m_{eff}L^2$,[42] we coarsely estimate the effective mass (m_{eff}) to be $0.9m_e$ with m_e being the electron mass for the holes given a QD of L = 40 nm. This estimate is larger than the reported values of $0.28m_e$[43] for holes in Ge/Si core/shell NWs and $0.08m_e$[18] obtained from Hall measurements on SiGe/Ge/SiGe planar junctions. Further experiments and analysis are required to more accurately determine m_{eff} in our device, which are beyond the scope of this paper.

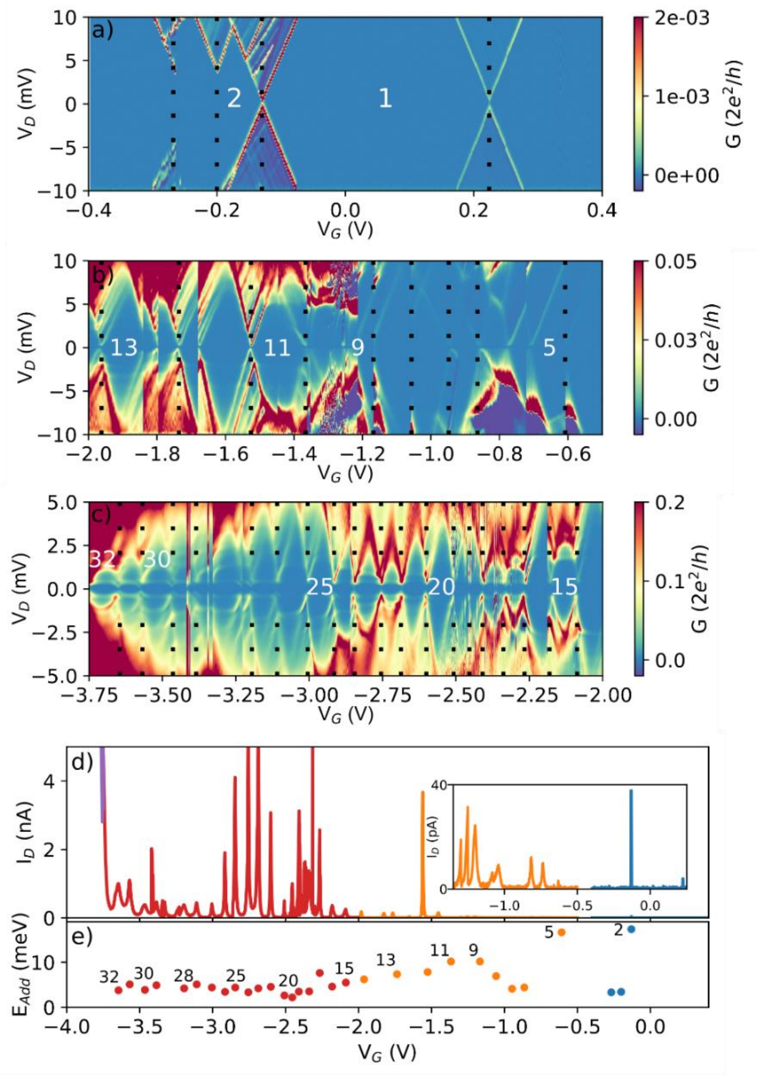

Figure 3. Stability diagram of the differential conductance (dI_D/dV_D) with respect to bias voltage (V_D) and gate voltage (V_G) in the Coulomb blockade regime: (a) In the first hole QD regime, (b) the few hole filling regime, (c) many hole filling regime. The numerical labels show the estimated number of holes (N) on the quantum dot (QD) for a sample of stable charge states. The black vertical dotted lines represent the charge degeneracy points where we estimate that a new hole has been introduced to the QD, while considering the occurrence of repeated or incomplete diamonds due to charge jumps. (d) I_D (V_G) slice at V_D = 0.48 mV. Each color represents a different measurement taken during the same cool-down (see Supplementary Information for details). (Inset) zoom of I_D (V_G) for 0.25 V < V_G < -1.45 V. (e) E_{Add}, calculated using $\alpha_G \Delta V_G$, versus V_G with sample of points labelled with the corresponding hole number (N).

2.4 Intermediate coupling regime

At a gate voltage of about V_G = - 3.8 V, CB features begin to fade out for $|V_D| > 2\Delta$. This is evident in Figure 3.d where the current rapidly diverges from the periodic current peaks of the CB regime, indicating the transition to the **intermediate coupling regime.** In **Figure 4**.b the differential conductance versus V_D and V_G is plotted. For V_G < -3.8 V, sub-gap conductance peaks with periodic modulation with respect to V_G appear. These resonances forming arcs bending towards zero-bias at the charge degeneracy points are interpreted as the experimental signature of single hole filling of the QD in the intermediate coupling regime. Similar to the CB regime, we estimate E_{add} (see Figure 4.a) and observe a continuation of the even-odd filling with comparable energies.

As the QD is filled with more holes, sub-gap features evolve; the magnitude of the conductance resonances increases and new conductance peaks emerge at lower bias voltages resulting in a reduction of the blockade region. This gate voltage dependence of the conductance peaks shows that these resonances are not simple multiple Andreev reflections (MAR) which should appear at constant bias voltage. In spectroscopy measurements performed on carbon nanotube QDs contacted by superconducting leads, such sub-gap facing bell-shaped resonances are associated with ABS which occur in a S-QD system in equilibrium through the coupling of discrete electronic states to the leads.[3]

The blue curves of Figure 4.c and 4.d show the current and the conductance as a function of the bias voltage for V_G adjusted to the degeneracy points (see vertical blue dashed line in Figure 4.b). The I-V measurements reveal a current peak at a bias voltage of about -160 µeV close to $\frac{2}{3}\Delta$ ~147 µeV. Related to this peak, negative conductance is observed in Figure 4.d. Such resonances have been predicted to occur in S-QD-S systems when Γ is of the order of

E_C[44] and result from the interplay between MAR resonances (the 3rd order occurs at $V_D \sim \frac{2}{3}\Delta$) with resonant tunneling.

Further, the resonant peak appears to be not symmetric with respect to V_D. Negative conductance shows up only at negative bias voltage and not at positive bias (blue curve). More interestingly, this asymmetry is inverted when a single hole is added inside the QD (red curve in Figure 4.c and Figure 4.d). As previously, we observe a current and negative conductance peak but this time at positive bias voltage. In combination, these individually asymmetric curves share significant symmetry: by reflecting the red G-V_D curve about the y-axis of V_D = 0 V we observe the underlying symmetry between the resonance features of the blue and red G-V_D curves (see Supporting Figure S12). The intriguing symmetry between the curves of two consecutive charge degeneracy points, that is observed in both samples, needs further investigation and measurements with a magnetic field or interface gates to confirm the nature of these transport characteristics.

These sub-gap bell-shaped resonances continue until V_G = -4.72 V where the low voltage blockade is replaced by a zero-bias conductance peak shown on Figure 4.e which we associate with superconducting transport across the QD. At lower gate voltage the intermediate regime shows regions of sub-gap features periodically separated by superconducting resonances until the supercurrent transport begins to overcome the blockade and large zero-bias conductance is observed continuously with respect to V_G marking the beginning of the supercurrent regime (see supporting Figure S11).

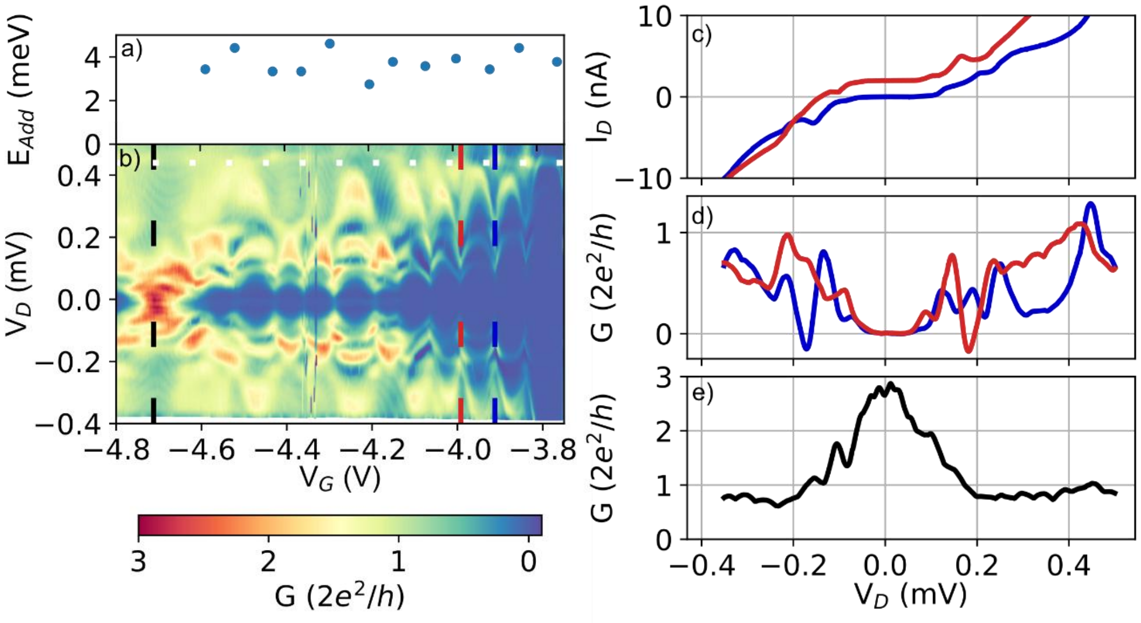

Figure 4. (a) E_{Add}, calculated using $\alpha_G \Delta V_G$, versus V_G. (b) Density plot of differential conductance with respect to bias voltage (V_D) and gate voltage (V_G) in the intermediate regime. White dashed line shows $eV_D = 2\Delta$ for $\Delta = 220$ μeV. We observe sub-gap conductance features that evolve with V_G. (c) I_D (V_D) & (d) G (V_D) slices at V_G = -3.91 V (dark blue) and V_G = -3.99 V (red). The red I_D (V_D) curve has been offset by +5 nA for clarity. (e) G (V_D) curve at V_G = -4.72 V.

2.5. Strong coupling regime

To investigate the supercurrent regime, current biasing measurements were carried out. **Figure 5**.a shows a density plot of the differential resistance (dV_D / dI_D) with respect to the current bias (I_D) and V_G across the device at 390 mK. Zero dV_D / dI_D observed for a range of bias currents I_D, symmetric around I_D = 0, indicate dissipationless transport through the Ge segment. Figure 5.b shows plots of V_D versus I_D at four gate voltages, highlighting the gate tunability and symmetry of the retrapping and critical current. For comparison, data for sample 2 is plotted in orange. We observe gate tunable critical current up to 10 nA for sample 1 and 6 nA for sample 2.

Outside this dissipationless current region (see Figure 5.a), we observe resonant features that are continuous with respect to V_G. To further understand these features, G versus V_D curves of the same data as Figure 5.b are plotted in Figure 5.c. The curves reveal that the resonant features are due to bias dependent conductance peaks, which are symmetric around a large zero-bias conductance peak corresponding to “infinite conductivity” of the supercurrent state. Further, the resonant features are consistent between samples 1 and 2. Considering that MAR is the cause of these conductance peaks, we superimpose on Figure5.c vertical dashed lines at the expected position $V_D = \frac{2\Delta}{ne}$ with $\Delta = \Delta^* = 185$ μeV being the superconducting gap and n being the MAR order. The clear alignment of up to three MAR conductance peaks with near constant V_D positions over a large gate range and across two independently measured samples highlights the quality of these heterostructures.

Δ^* agrees with the extracted Δ from MAR in Al-Ge/Si-Al core/shell NWs that had similar Al leads,[28] however, differs significantly from the Δ = 220 +/- μeV extracted in the CB regime. This difference is understood to be due to the reduction of the superconducting gap at the Al-Ge interface resulting from the exchange of charge between the normal conductor and superconductor. This so-called inverse-proximity effect on the superconductor poisons the superconducting gap in the region that is in close proximity to the normal metal, thus reducing the magnitude of Δ,[46] which we refer to as a renormalized gap (Δ^*). The absence of the Schottky barrier in the strong coupling regime permits the inverse-proximity effect through the interaction of the QD and superconducting leads, thus resulting in the observations of a renormalised gap of $\Delta^* = 185$ μeV, which is, as expected, less than the BCS gap.

In the weak coupling regime of our intrinsic Ge system the strong agreement between the measured Δ = 220 μeV with the BCS gap of 222 μeV suggests there is no renormalization of the superconducting gap. Indeed in this regime the Schottky barrier at the Al-Ge interface acts as an insulating barrier isolating the QD from the superconducting leads. This isolation prevents the inverse proximity effect and thus prevents the renormalisation of Δ.

The observation of MAR singularities in the supercurrent regime promotes the use of a Monte-Carlo based fitting algorithm which by fitting the non-linear I-V curves provides an estimate of the number of conduction channels and the transparency of each channel.[47] The fits of the curves of V_G = -8.6 V and V_G = -15.5 V (see supporting Figure S14) provide similar high transparencies of the first channel of 95% and 96% respectively. Consistent with the transport properties of a majority hole carrier semiconductor more conduction channels contribute to the transport at V_G = -15.5 V than V_G = -8.6 V (see supporting Figure S15 for a bar chart of the respective channel transparencies). Further, the transparency of the mutually active channels (2, 3, 4) are significantly higher at V_G = -15.5 V than V_G = -8.6 V suggesting that the conduction channels are not fully open when a new channel becomes available. Nonetheless, the high transparency of the first and second channel in the case of V_G = -15.5 V endorses the high quality of these heterostructures. Such transparencies can be compared to the results of the BTK model,[48] which is often used to estimate the average contact transparency of SNS junctions. The same V_G slices -8.6 V and -15.5 V yield approximate transparencies of 60% and 90%, respectively. Though differing from the transparency results of the first channel obtained from the MAR fits, a quantitative agreement with the BTK model is obtained by taking an average of the transparencies of the first three channels, giving 60% for V_G = -8.6 V and 80% for V_G = -15.5 V.

In the ballistic regime, the superconducting coherence length of an SNS junction is given by $\xi_S = \frac{\hbar v_F}{\pi \Delta}$ where v_F is the Fermi velocity of the semiconductor and Δ is the superconducting gap of 220 µeV. Assuming the minimum Fermi energy (E_F) of 10 meV to be the energy of the first sub-band which is estimated from the energy levels of the 1D modes in the Ge nanowire due to radial confinement[43] and a maximum effective mass of heavy-holes m_{HH} of $0.28m_0$ we estimate a minimum $v_F = \sqrt{2E_F/m_{HH}}$ of 1.1 x 10^5 ms^{-1}. This results in a superconducting coherence length of approximately 110 nm, which puts the system in the short junction limit with $L_{Ge} << \xi_S$. However, as $L_{Ge} \sim \ell_{Ge}$ it is difficult to define whether the junction is in the clean or dirty limit. Interestingly, the 'Figure of merit' product I_CR_N, where R_N is the normal resistance gives 25 μV and 16 μV for slices V_G = -15.5 V and V_G = -8.6 V respectively. For an SNS junction in the regime $L_{Ge} << \xi_S$ the gap is related to the I_CR_N product by $eI_CR_N = \pi\Delta$. The product values are 20 and 30 times smaller than Δ suggesting that I_C is considerably suppressed possibly due to residual measurement noise and/or thermal fluctuation at T = 390 mK overcoming the Josephson energy $\frac{\hbar}{2e}I_c$.

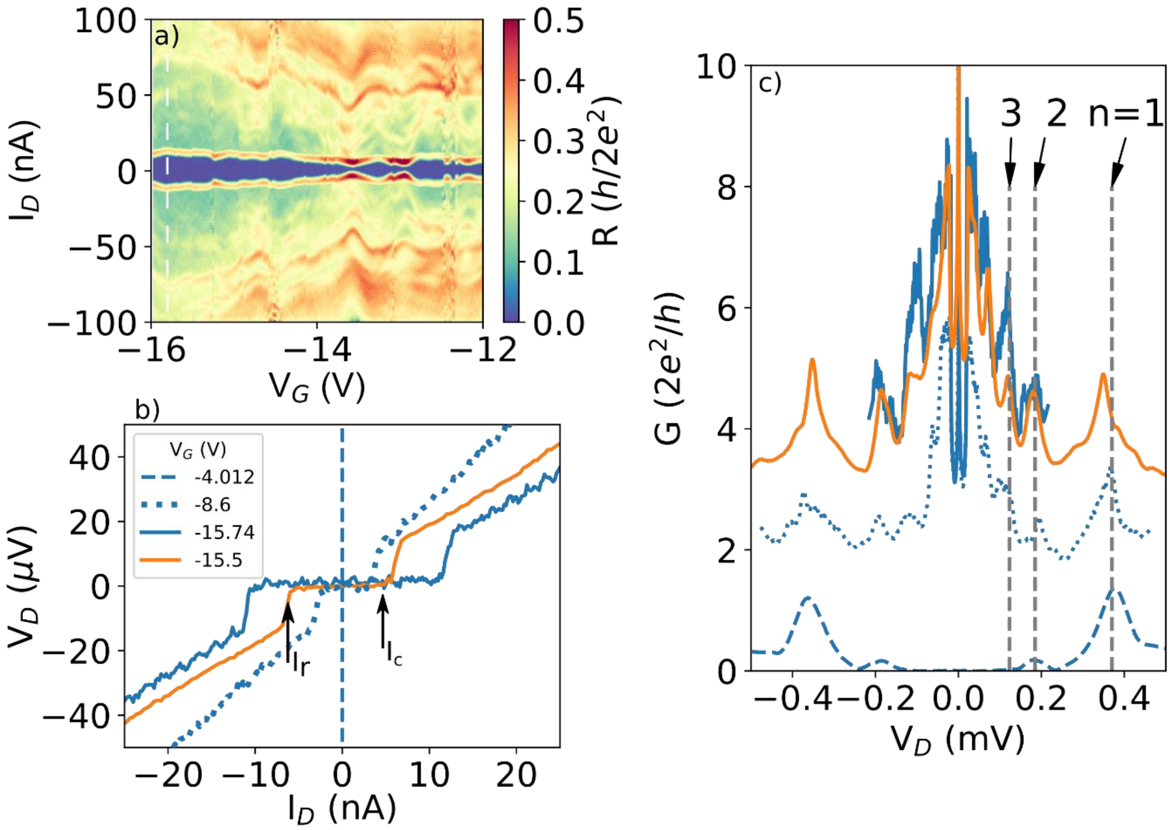

Figure 5. (a) Density plot of differential resistance (dV_D/dI_D) with respect to bias current (I_D) and gate voltage (V_G) in the superconducting regime showing the gate dependent supercurrent and MAR resonances. (b) V_D versus I_D for four V_G slices showing the onset of supercurrent. For comparison both Sample 1 (blue curves) and Sample 2 are shown (orange curve). Retrapping (I_r) and critical current (I_c) are labelled. (c) G (V_D) curves for the same V_G slices of (b); we see clear conductance peaks which we associate with MAR. The vertical grey dashed lines indicate the expected voltage position ($V_n = 2\Delta/ne$) of the first three MAR peaks for $\Delta = \Delta^{*}$ 185 μeV.

3. Conclusion

In conclusion, we have reported on the low temperature transport properties of monolithic Al-Ge-Al NW heterostructures with i-Ge segments of lengths of 42 nm and 37 nm. We have shown that the thermal exchange fabrication technique produces heterostructures with high material quality, reproducibility and controllable Ge segments with high transparency of the

Al-Ge interface (up to 96%). Using a single back gate, we can tune the system from a single-hole filling quantum dot regime with charging energies up to 30 meV to a superconducting regime with tunable supercurrent up to 10 nA. This tunability facilitates the use of our system as a building block for the realization of a gatemon. Moreover, the subtle interplay between CB and Andreev mediated superconductivity in germanium QDs provides rich physics and a promising platform for the study of Majorana Fermions. These results add further weight to the growing evidence that Ge has significant potential as a key material in future quantum technologies.

4. Experimental Section/Methods

Ge NW synthesis

The Ge NWs were grown on Si (111) substrates using the VLS process with germane (GeH_4, 2% diluted in He) as precursor and a 2 nm thick sputtered Au layer as the 1D growth promoting catalyst. The actual growth was performed in a low pressure hot wall CVD chamber at 50 mbar and a gas flow of 100 sccm for both, the precursor gas and H_2 as carrier gas. After the pressure and precursor flow is stable, the temperature was ramped up at a rate of 60 K/min to the target temperature of 613 K. The rather high growth temperature ensures uniform catalyst diameter and good NW epitaxy. After a 10 min nucleation phase, the temperature is lowered to 573 K. Typical growth duration of 60 min result in 8 µm long NWs and uniform diameters of about 25 nm. Subsequently to the growth, the NWs were uniformly coated with 20 nm Al_2O_3 by atomic layer deposition.

Al-Ge-Al device fabrication

The starting materials are VLS grown intentionally undoped Ge NWs with a diameter of 25 nm enwrapped in a 20 nm thick Al_2O_3 passivating shell. The NWs were drop casted onto an oxidized highly *p*-doped Si substrate and the Ge core NW was contacted by Al pads fabricated by electron beam lithography, 100 nm Al sputter deposition and lift-off techniques. Prior to the Al deposition a two step wet chemical etching was performed. First, to gain access to the Ge core NW the Al_2O_3 shell was selectively removed by a 22 s dip in BHF (7%). Secondly, to remove the native Ge oxide layer formed underneath the Al_2O_3 shell, a 5s HI dip (14%) was applied. The Al-Ge exchange reaction is induced by rapid thermal annealing at a temperature of T = 674 K in forming gas atmosphere and results in the substitution of the Ge core by c-Al[27].

Electrical characterisation

The electrical measurements were carried out using a self-built pumped ^{3}He cryostat with a minimum temperature of T = 340 mK. Noise filtering was achieved using a room temperature Pi-filter and at low temperature thermal coax of approximately 1 m in length. The device was measured using a two probe technique at low temperature using both voltage and current biasing techniques with a National Instruments PCI DAC/ADC high frequency card. The resistance of the fridge wiring was independently measured to be 390 Ω at 390 mK for which the data has been corrected for. In the voltage biasing scheme a voltage divider consisting of 50kΩ / 50Ω was used to reduce the amplitude of the voltage source. A Femto variable gain transimpedance amplifier (DCPCA-200) was used to convert and amplify the induced current to a voltage signal measured by the NI card. In the current biasing scheme a 10 MΩ resistor was used to convert the voltage signal to a current signal with a maximum amplitude of 1 µA. The current was applied to the sample which was grounded at one end. The potential difference across the sample was amplified by two NF Electronic Instruments low noise preamplifiers (LI-75A), each of a gain of 100, in series. The back-gate was biased using a Yokogawa programmable voltage source. Measurements were taken with a range of bias voltages/currents, gate voltages and gains of the transimpedance amplifier. The parameters of each measurement used for discussion in the paper are detailed in the Supporting Information.

Supporting Information

Supporting Information is available from the Wiley Online Library or from the author.

Acknowledgements

The authors would like to acknowledge S. De Franceschi, F. Lefloch, D. Basko, K. Rafsanjani, D. Szombati and T. Vethaak for beneficial discussions. The authors gratefully acknowledge financial support by the Austrian Science Fund (FWF): project No. P29729-

N27. The authors further thank the Center for Micro- and Nanostructures for providing the cleanroom facilities. We acknowledge support from the Laboratoire d'excellence LANEF in Grenoble (ANR-10-LABX-51-01). Financial support from the ANR-COSMOS (ANR-12-JS10-0002) project and ANR-QPSNWs (ANR-15-CE30-0021) project is acknowledged. We acknowledge support from Campus France in the framework of PHC AMADEUS 2016 for PROJET N° 35592PB. J. Delaforce acknowledges the European Union's Horizon 2020 research and innovation programme under the Marie Skłodowska-Curie grant agreement No 754303. This project has also received funding from the European Research Council under the European Union's H2020 Research and Innovation programme *via* the e-See project (grant #758385). We benefitted from the access to the Nano characterization platform (PFNC) in CEA Minatec Grenoble.

Conflict of Interest

The authors declare no conflict of interest.

References

[1] S. De Franceschi, L. Kouwenhoven, C. Schönenberger, W. Wernsdorfer, *Nature Nanotechnology* **2010**, *5*, 703.

[2] A. Eichler, M. Weiss, S. Oberholzer, C. Schönenberger, A. Levy Yeyati, J. C. Cuevas, A. Martín-Rodero, *Physical Review Letters* **2007**, *99*, DOI 10.1103/PhysRevLett.99.126602.

[3] J.-D. Pillet, C. H. L. Quay, P. Morfin, C. Bena, A. L. Yeyati, P. Joyez, *Nature Phys* **2010**, *6*, 965.

[4] H. B. Heersche, P. Jarillo-Herrero, J. B. Oostinga, L. M. K. Vandersypen, A. F. Morpurgo, *Nature* **2007**, *446*, 56.

[5] M. R. Sahu, X. Liu, A. K. Paul, S. Das, P. Raychaudhuri, J. K. Jain, A. Das, *Phys. Rev. Lett.* **2018**, *121*, 086809.

[6] V. Mourik, K. Zuo, S. M. Frolov, S. R. Plissard, E. P. A. M. Bakkers, L. P. Kouwenhoven, *Science* **2012**, *336*, 1003.

[7] Ö. Gül, H. Zhang, F. K. de Vries, J. van Veen, K. Zuo, V. Mourik, S. Conesa-Boj, M. P. Nowak, D. J. van Woerkom, M. Quintero-Pérez, M. C. Cassidy, A. Geresdi, S. Koelling,

D. Car, S. R. Plissard, E. P. A. M. Bakkers, L. P. Kouwenhoven, *Nano Letters* **2017**, *17*, 2690.

[8] Y.-J. Doh, J. A. van Dam, A. L. Roest, E. P. A. M. Bakkers, L. P. Kouwenhoven, S. De Franceschi, *Science* **2005**, *309*, 272.

[9] W. Chang, S. M. Albrecht, T. S. Jespersen, F. Kuemmeth, P. Krogstrup, J. Nygård, C. M. Marcus, *Nature Nanotechnology* **2015**, *10*, 232.

[10] K. Gharavi, G. W. Holloway, R. R. LaPierre, J. Baugh, *Nanotechnology* **2017**, *28*, 085202.

[11] L. Tosi, C. Metzger, M. F. Goffman, C. Urbina, H. Pothier, S. Park, A. L. Yeyati, J. Nygård, P. Krogstrup, *Phys. Rev. X* **2019**, *9*, 011010.

[12] M. Tinkham, *Introduction to Superconductivity*, Dover Publications, **2004**.

[13] T. W. Larsen, K. D. Petersson, F. Kuemmeth, T. S. Jespersen, P. Krogstrup, J. Nygård, C. M. Marcus, *Physical Review Letters* **2015**, *115*, DOI 10.1103/PhysRevLett.115.127001.

[14] J. Xiang, A. Vidan, M. Tinkham, R. M. Westervelt, C. M. Lieber, *Nature Nanotechnology* **2006**, *1*, 208.

[15] F. K. de Vries, J. Shen, R. J. Skolasinski, M. P. Nowak, D. Varjas, L. Wang, M. Wimmer, J. Ridderbos, F. A. Zwanenburg, A. Li, S. Koelling, M. A. Verheijen, E. P. A. M. Bakkers, L. P. Kouwenhoven, *Nano Letters* **2018**, *18*, 6483.

[16] J. Ridderbos, M. Brauns, J. Shen, F. K. de Vries, A. Li, E. P. A. M. Bakkers, A. Brinkman, F. A. Zwanenburg, *Adv. Mater.* **2018**, *30*, 1802257.

[17] J. Ridderbos, M. Brauns, A. Li, E. P. A. M. Bakkers, A. Brinkman, W. G. van der Wiel, F. A. Zwanenburg, *Physical Review Materials* **2019**, *3*, DOI 10.1103/PhysRevMaterials.3.084803.

[18] N. W. Hendrickx, D. P. Franke, A. Sammak, M. Kouwenhoven, D. Sabbagh, L. Yeoh, R. Li, M. L. V. Tagliaferri, M. Virgilio, G. Capellini, G. Scappucci, M. Veldhorst, *Nature Communications* **2018**, *9*, 2835.

[19] F. Vigneau, R. Mizokuchi, D. C. Zanuz, X. Huang, S. Tan, R. Maurand, S. Frolov, A. Sammak, G. Scappucci, F. Lefloch, S. De Franceschi, *Nano Letters* **2019**, *19*, 1023.

[20] H. Watzinger, C. Kloeffel, L. Vukušić, M. D. Rossell, V. Sessi, J. Kukučka, R. Kirchschlager, E. Lausecker, A. Truhlar, M. Glaser, A. Rastelli, A. Fuhrer, D. Loss, G. Katsaros, *Nano Letters* **2016**, *16*, 6879.

[21] A. Dimoulas, P. Tsipas, A. Sotiropoulos, E. K. Evangelou, *Applied Physics Letters* **2006**, *89*, 252110.

[22] A. Thanailakis, D. C. Northrop, *Solid-State Electronics* **1973**, *16*, 1383.

[23] N. Neophytou, Jing Guo, M. S. Lundstrom, *IEEE Trans. Nanotechnology* **2006**, *5*, 385.

[24] T. Burchhart, A. Lugstein, C. Zeiner, Y. J. Hyun, G. Hochleitner, E. Bertagnolli, *Elektrotech. Inftech.* **2010**, *127*, 171.

[25] M. Sistani, P. Staudinger, J. Greil, M. Holzbauer, H. Detz, E. Bertagnolli, A. Lugstein, *Nano Letters* **2017**, *17*, 4556.

[26] M. A. Luong, E. Robin, N. Pauc, P. Gentile, M. Sistani, A. Lugstein, M. Spies, B. Fernandez, M. I. Den Hertog, *ACS Appl. Nano Mater.* **2020**, *3*, 1891.

[27] S. Kral, C. Zeiner, M. Stöger-Pollach, E. Bertagnolli, M. I. den Hertog, M. Lopez-Haro, E. Robin, K. El Hajraoui, A. Lugstein, *Nano Letters* **2015**, *15*, 4783.

[28] M. Sistani, J. Delaforce, R. B. G. Kramer, N. Roch, M. A. Luong, M. I. den Hertog, E. Robin, J. Smoliner, J. Yao, C. M. Lieber, C. Naud, A. Lugstein, O. Buisson, *ACS Nano* **2019**, *13*, 14145.

[29] M. Sistani, J. Delaforce, K. Bharadwaj, M. Luong, J. Nacenta Mendivil, N. Roch, M. den Hertog, R. B. G. Kramer, O. Buisson, A. Lugstein, C. Naud, *Appl. Phys. Lett.* **2020**, *116*, 013105.

[30] J. Ridderbos, M. Brauns, F. K. de Vries, J. Shen, A. Li, S. Kölling, M. A. Verheijen, A. Brinkman, W. G. van der Wiel, E. P. A. M. Bakkers, F. A. Zwanenburg, *Nano Letters* **2020**, *20*, 122.

[31] K. El hajraoui, M. A. Luong, E. Robin, F. Brunbauer, C. Zeiner, A. Lugstein, P. Gentile, J.-L. Rouvière, M. Den Hertog, *Nano Letters* **2019**, *19*, 2897.

[32] M. A. Luong, E. Robin, N. Pauc, P. Gentile, T. Baron, B. Salem, M. Sistani, A. Lugstein, M. Spies, B. Fernandez, M. den Hertog, *ACS Appl. Nano Mater.* **2020**, *3*, 10427.

[33] M. Spies, Z. Sadre Momtaz, J. Lähnemann, M. Anh Luong, B. Fernandez, T. Fournier, E. Monroy, M. I den Hertog, *Nanotechnology* **2020**, *31*, 472001.

[34] M. Sistani, P. Staudinger, A. Lugstein, *J. Phys. Chem. C* **2020**, *124*, 19858.

[35] S. Zhang, E. R. Hemesath, D. E. Perea, E. Wijaya, J. L. Lensch-Falk, L. J. Lauhon, *Nano Lett.* **2009**, *9*, 3268.

[36] R. Pillarisetty, *Nature* **2011**, *479*, 324.

[37] H. Tahini, A. Chroneos, R. W. Grimes, U. Schwingenschlögl, A. Dimoulas, *J. Phys.: Condens. Matter* **2012**, *24*, 195802.

[38] J. Xiang, W. Lu, Y. Hu, Y. Wu, H. Yan, C. M. Lieber, *Nature* **2006**, *441*, 489.

[39] R. Hanson, L. P. Kouwenhoven, J. R. Petta, S. Tarucha, L. M. K. Vandersypen, *Reviews of Modern Physics* **2007**, *79*, 1217.

[40] G. Katsaros, P. Spathis, M. Stoffel, F. Fournel, M. Mongillo, V. Bouchiat, F. Lefloch, A. Rastelli, O. G. Schmidt, S. De Franceschi, *Nature Nanotechnology* **2010**, *5*, 458.

[41] F. M. Brunbauer, E. Bertagnolli, J. Majer, A. Lugstein, *Nanotechnology* **2016**, *27*, 385704.

[42] F. A. Zwanenburg, A. A. van Loon, G. A. Steele, C. E. W. M. van Rijmenam, T. Balder, Y. Fang, C. M. Lieber, L. P. Kouwenhoven, *Journal of Applied Physics* **2009**, *105*, 124314.

[43] W. Lu, J. Xiang, B. P. Timko, Y. Wu, C. M. Lieber, *PNAS* **2005**, *102*, 10046.

[44] A. L. Yeyati, J. C. Cuevas, A. López-Dávalos, A. Martín-Rodero, *Phys. Rev. B* **1997**, *55*, R6137.

[45] B.-K. Kim, Y.-H. Ahn, J.-J. Kim, M.-S. Choi, M.-H. Bae, K. Kang, J. S. Lim, R. López, N. Kim, *Phys. Rev. Lett.* **2013**, *110*, 076803.

[46] A. A. Kopasov, I. M. Khaymovich, A. S. Mel’nikov, *Beilstein J. Nanotechnol.* **2018**, *9*, 1184.

[47] J. J. Riquelme, L. de la Vega, A. L. Yeyati, N. Agraït, A. Martin-Rodero, G. Rubio-Bollinger, *Europhysics Letters (EPL)* **2005**, *70*, 663.

[48] G. E. Blonder, M. Tinkham, T. M. Klapwijk, *Physical Review B* **1982**, *25*, 4515.